commensurate and incommensurate phases, which we observed in the powder XRD patterns of 2-undecanone/urea and 6-undecanone/urea. Other phenomena, such as dislocation effects on the positions of the Bragg maxima, have not yet been documented. See (6) and B. E. Warren, *Phys. Rev.* **59**, 693 (1941).

19. The much weaker 3D ordering (with $\Delta_g = 0$ Å) (6) of guests in linear alkane/UICs can be understood in terms of the same commensurate structures. [The guest repeats for alkanone/UICs (Table 1) are all within 0.1 Å of those reported for the analogous alkane/UICs. See H. U. Lenné, H. C. Mez, W. Schlenk Jr., *Justus Liebigs Ann. Chem.* **732**, 70 (1970).]

20. To our knowledge, only UICs containing guests with $\Delta_g = 0$ Å grow as {001} plates.

21. This common theme of bridging ureas is repeated in the crystal structure of 2,7-octanedione/urea. In this context, the pronounced interchannel ordering and extremely low aspect ratio for 2-tridecanone/urea (Table 1) can be seen as a special consequence of the commensurate relation ($3c'_g = 5c'_h$), the bridging by ureas of the terminal methyl ketone groups, and the long chain length of the guest (which inhibits guest protrusion).

22. In cases for which co-inclusion of guests is possible (such as mixtures of 2-undecanone and 6-undecanone), the 3D ordering of guests is diminished considerably, and needles are favored.

23. By solid-state NMR (12) and XRD, which probe intra- and interchannel ordering of guests, the needles and plates are structurally indistinguishable.

24. Mean aspect ratios for 2-dodecanone/urea and 2-undecanone/urea grown from isobutyl alcohol were 6 ± 2 and 13 ± 7, respectively. See (2) for an alternative role of solvent molecules.

25. In conjunction with this solvent dependence and (22), we note that the most dramatic example of habit modification we have observed occurred with mixed UICs of 1,10-dichlorodecane and 1,10-dicyanodecane grown from a 7:1 mixture of the guests and urea in isobutyl alcohol; the aspect ratios for these crystals were remarkably high and ranged from 500 to 2500.

26. The delicate nature of the {001} surfaces of 2-decanone/urea crystals resulted in continual etching during imaging, which prevented an accurate picture of the surface topography.

27. H. C. Chang, R. Popovitz-Biro, M. Lahav, L. Leiserowitz, *J. Am. Chem. Soc.* **104**, 614 (1982).

28. We have not yet determined the crystal structures of 2,12-tridecanedione/urea or 2,13-tetradecanedione/urea, so the presence of true crystallographic threefold or sixfold screw axes for these systems is still in question. For C_9 and C_{12} diketones, the metric properties of the diffraction patterns do not allow us to make alternative supercells with $9c'_g = 11c'_h$ (C_9) and $7c'_g = 11c'_h$ (C_{12}), but the oscillation photographs strongly favor the commensurate relations.

29. C. K. Johnson, *Rep. ORNL-3794* (Oak Ridge National Laboratory, Oak Ridge, TN, 1965).

30. We thank C. R. Goss, C. J. Nichols, M. D. Ward, A. E. Aliev, and K. D. M. Harris for their help with this work, and J. M. McBride for critical comments on the manuscript. This work was supported by the National Science and Engineering Research Council (Canada), the Petroleum Research Fund (administered by the American Chemical Society), the National Science Foundation (CHE-9423726), and the Alfred P. Sloan Foundation (fellowship to M.D.H.).

20 March 1996; accepted 3 July 1996

Mantle Viscosity and Ice-Age Ice Sheet Topography

W. Richard Peltier

Ice-age paleotopography and mantle viscosity can both be inferred from observations of Earth's response to the most recent deglaciation event of the current ice age. This procedure requires iterative application of a theoretical model of the global process of glacial isostatic adjustment. Results demonstrate that the iterative inversion procedure converges to a paleotopography that is extremely close to that from the ICE-4G model. The accompanying mantle viscosity profile is furthermore shown to reconcile the requirements of aspherical geoid anomalies related to the mantle convection process, thus resolving a fundamental issue concerning mantle rheology. The combined model also explains postglacial sea level histories for the east coast of the United States.

$\mathbf{G}$lobal signatures of the glacial isostatic adjustment (GIA) process constrain both the viscosity of Earth's mantle and the weight of the extensive continental ice sheets that existed on Earth's surface at the last glacial maximum (LGM). The theory that has been developed to describe the GIA process (1, 2) involves only these two unknowns, as the elastic structure of the spherically symmetric viscoelastic model Earth is assumed to be fixed to that of the seismologically constrained PREM (3). The problem of applying this theory to infer both deglaciation history and mantle viscosity on the basis of the observed response to deglaciation is nonlinear. Errors in our knowledge of either mantle viscosity or deglaciation history could, in principle, propagate into our inference of the other. The widely varying inferences of mantle viscosity that have appeared in recent literature could thus be a simple consequence of er-

Department of Physics, University of Toronto, Toronto, Ontario, Canada M5S 1A7.

rors in the deglaciation history (4). Similarly, recently proposed models of the deglaciation history may be sensitive [for example, see (5)] to errors in the model of the radial variation of viscosity. Here I show that the iterative solution of this nonlinear problem converges to acceptably stable estimates of both mantle viscosity and deglaciation history and that the global model of GIA so constrained reconciles the observed postglacial relative sea level (rsl) history along the east coast of the North American continent for the first time.

As a starting point, I used the recently derived ICE-4G model of the history of deglaciation since the LGM (1). The variations in continental ice sheet thickness in this model were derived by inverting postglacial rsl histories through the use of a simple radial profile of mantle viscosity (referred to herein as M1), a three-layer model incorporating a lithosphere of thickness 120.6 km, an upper mantle and transition zone with a viscosity of 10^{21} Pa·s, and a lower mantle with a viscosity of 2×10^{21}

Pa·s. In the family of simple three-layer parameterizations, this structure is the globally preferred structure (6, 7) when the viscosity of the upper mantle and transition zone is fixed to the nominal value of 10^{21} Pa·s originally inferred by Haskell (8) on the basis of his analysis of the postglacial rebound of Fennoscandia. The ICE-4G deglaciation history differs significantly from that of CLIMAP (9) and is currently in use internationally as a lower boundary condition for a new generation of atmospheric general circulation model reconstructions of LGM climate. The issue of the validity of ICE-4G is therefore rather important. I investigate this matter by fixing the deglaciation history to ICE-4G and then refining the viscosity profile by applying well-established formal procedures. The refined viscosity profile (M2) was then used to recompute the response to deglaciation on which basis the ICE-4G model was originally inferred to demonstrate that full convergence of the solution is obtained with minor modification to ICE-4G.

Mantle viscosity from GIA. The formal procedure used to refine M1 was developed in a series of recent articles (10–12) in which the methodology of Bayesian inference (13) plays a critical role. The data (11, 12) include the relaxation spectrum for the postglacial rebound of Fennoscandia (14) (see Fig. 3B for a plot of the spectrum) and site-specific relaxation times inferred from ^{14}C-dated emergence histories from six sites surrounding the Gulf of Bothnia, seven sites surrounding Hudson Bay, and 10 sites in the Canadian Arctic (Fig. 1, A and B). The formal inversion is also constrained by two anomalies of Earth's present rotational state (11): the ongoing wander of the planet's axis of rotation at the rate of ~0.95° per million years along the 76°W meridian and the so-called nontidal acceleration of the rate of axial rotation. This nontidal accel-

eration corresponds to a rate of change of the degree-two zonal harmonic of the gravitational potential, $\dot{J}_2$, in the range -2.5×10^{-11} to -3.5×10^{-11} year^{-1} (11). With the exception of these rotational constraints, the data in this set are either independent (the Fennoscandian relaxation spectrum) or only weakly dependent (site-specific relaxation times) on the history of surface loading (10). Such data therefore provide a means of suppressing the nonlinearity of the inverse problem through which errors in the loading history can propagate into errors in the inference of viscosity.

Each of these measures of the response of the planet to the last deglaciation event of the current ice age may be related to the mantle viscosity profile through a relation of the form
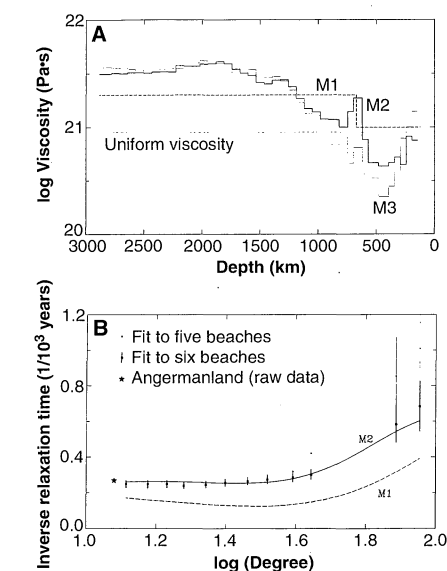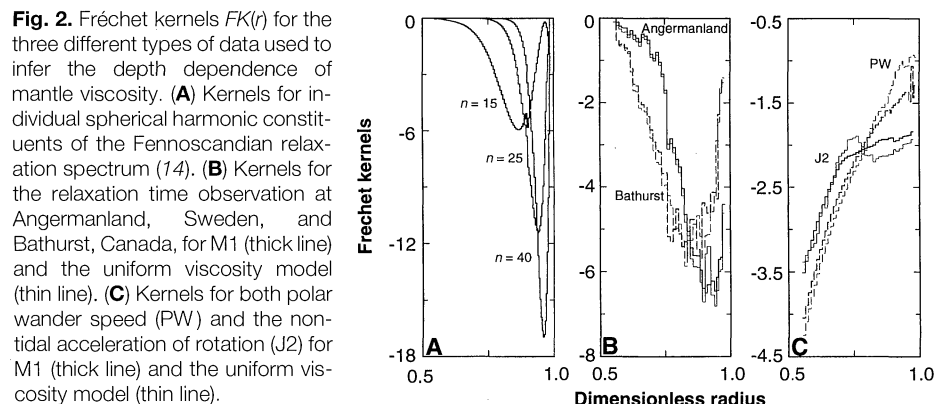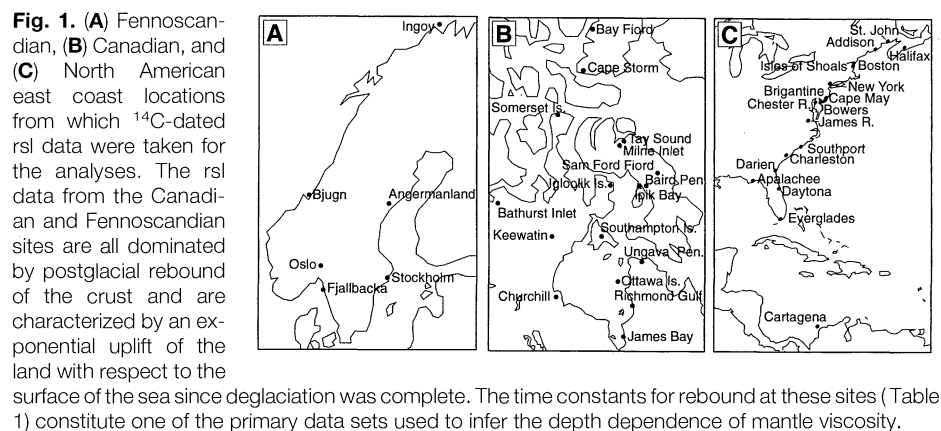
$$\delta R = \int_b^a r^2 \, FK(r) \, \delta \log \nu(r) \, dr \qquad (1)$$

in which δR is the variation of the response that is induced by a variation in the radial profile of mantle viscosity $\nu(r)$ (parameterized in terms of its logarithm). The functions $FK(r)$ are the Fréchet kernels (13), which measure the sensitivity of the response to depth-dependent variations of viscosity. For the individual components of the Fen-noscandian relaxation spectrum, the values of $FK(r)$ have been derived analytically on the basis of a viscoelastic extension of Rayleigh's variational principle of elasticity (15). For both the site-specific relaxation times and the rotational data, the values of $FK(r)$ must be determined by direct numerical analysis based on the construction of multiple solutions of the forward problem for postglacial rsl history (10) using the theory described in (1, 2). The Fréchet kernels for all three data types are complementary (Fig. 2): (i) The Fennoscandian relaxation spectrum provides excellent coverage of the upper mantle and transition zone; (ii) the site-specific relaxation time data extend this sensitivity into the lower mantle, with the maximum sensitivity of Fennoscandian data residing in the transition zone and the maximum sensitivity of the Laurentide data residing in the upper part of the lower mantle; and (iii) the rotational data provide sensitivity from the surface to the core-mantle boundary. The depths of maximum sensitivity of the site-specific relaxation times from central Fennoscandia (Angermanland) and Canada (Bathurst Inlet), revealed by inspection of the Fréchet derivatives, demonstrate this differential sensitivity. It is precisely because of the complementary nature of these data, along with their weak dependence on deglaciation history (the rotational data do not share this characteristic), that makes the combination of them so useful for mantle viscosity inference. We have also computed the Fréchet derivatives for two different starting models. One is M1, and the other is a model with a uniform mantle viscosity of 0.9 $\times$ 10^{21} Pa·s from the base of the lithosphere to the core-mantle boundary and a lithospheric thickness of 120.6 km. Comparison of the kernels for these two starting models (Fig. 2, B and C) provides a measure of the extent to which the inverse problem for viscosity has been successfully linearized through use of the logarithmic parameterization.

The radial profiles of mantle viscosity obtained from the formal inversion of all of the data (Fig. 3A) are essentially the same, independent of the starting model. The Fennoscandian relaxation spectrum constrains the upper mantle and transition zone viscosity to ~0.4 $\times$ 10^{21} Pa·s, slightly lower than the nominal value of 10^{21} Pa·s originally inferred by Haskell (8). Below the 660-km discontinuity, the viscosity rises somewhat, but less so than in many early analyses (16) based on nonhydrostatic geoid data. The inversions initialized with M1 and the uniform-viscosity model (called M2 and M3, respectively) deliver radial variations of mantle viscosity whose averages from the base of the lithosphere to a depth of 1171 km (a radius of 5200 km) are, respectively,

Fig. 1. (**A**) Fennoscandian, (**B**) Canadian, and (**C**) North American east coast locations from which ^{14}C-dated rsl data were taken for the analyses. The rsl data from the Canadian and Fennoscandian sites are all dominated by postglacial rebound of the crust and are characterized by an exponential uplift of the land with respect to the surface of the sea since deglaciation was complete. The time constants for rebound at these sites (Table 1) constitute one of the primary data sets used to infer the depth dependence of mantle viscosity.

Fig. 2. Fréchet kernels $FK(r)$ for the three different types of data used to infer the depth dependence of mantle viscosity. (**A**) Kernels for individual spherical harmonic constituents of the Fennoscandian relaxation spectrum (14). (**B**) Kernels for the relaxation time observation at Angermanland, Sweden, and Bathurst, Canada, for M1 (thick line) and the uniform viscosity model (thin line). (**C**) Kernels for both polar wander speed (PW) and the nontidal acceleration of rotation (J2) for M1 (thick line) and the uniform viscosity model (thin line).

Fig. 3. (**A**) The a posteriori viscosity models obtained by simultaneously inverting all three data sets for which sample Fréchet derivatives are shown in Fig. 2. (**B**) The McConnell (14) relaxation spectrum for Fennoscandia (symbols) compared with the fit achieved with models M1 and M2 (lines). The misfit at high wave number suggests that the viscosity in the immediately sublithospheric region may have to be further reduced.

0.87 $\times$ 10^{21} and 0.76 $\times$ 10^{21} Pa·s. The difference between each of these values and the nominal viscosity inferred by Haskell (8) is small. No pronounced increase of viscosity across the 660-km discontinuity exists in these models, and any such variation in the radial average over a length scale of 500 km or greater on either side of this horizon is ruled out. This result is in accord with many earlier analyses of glacial rebound data (17). Comparison of the two final models shows that the thin high-viscosity feature near the 660-km discontinuity in the M2 model is an artifact of the step discontinuity in viscosity that characterized M1 at this depth. The existence of a feature of this kind is not ruled out by the data, however, and because such a feature might be expected on physical grounds if the convective circulation were episodically layered by the influence of the 660-km phase transformation [see (18) for a discussion], models in this class are especially interesting. Models with a thin low-viscosity layer directly above the 660-km discontinuity (19) are also not excluded.

In both inversions, the viscosity of the mantle below a depth of about 1200 km is inferred to be ~3.5 $\times$ 10^{21} Pa·s. A higher viscosity would be inferred for the lower 800 km of the mantle if we were to include the influence on the rotational data of contamination associated with the present-day melting of land ice on Antarctica and Greenland (11, 12). The viscosity in this lowermost region of the lower mantle could therefore be as high as 10^{22} Pa·s. The best two-layer approximation to the M2-M3 average would have the interface near a depth of 1170 km and an increase in viscosity by a factor of 4 across it. This two-layer model is similar to M1, in which the interface was assumed to occur at the depth of the 660-km discontinuity and the increase to be by a factor of 2 from the nominal Haskell value of 10^{21} Pa·s. That the increased depth to the region of higher viscosity in the formally derived models should be accompanied by an increase in the viscosity enhancement is clear on the simplest physical grounds. The viscosity increases across the entire mantle in these models, from the region immediately beneath the lithosphere to the core-mantle boundary, by a factor of 10 to 20.

Comparison of the Fennoscandian relaxation spectrum (14) with the fit to this spectrum achieved with viscosity models M1 and M2 (Fig. 3B) demonstrates that M1 predicts relaxation times that are excessively high for all wave numbers, whereas M2 fits the observed spectrum extremely well at the longest wavelengths. The critical wave number beyond which relaxation times decrease is strongly controlled by lithospheric thickness; this property of the observed spectrum is also well fit by M2, although the shortest relax-

ation times are not, because only the relaxation times in the stable long-wavelength tail of the spectrum were used in the formal inversion. Also shown in Fig. 3B is the relaxation time deduced by Monte Carlo fit to the rsl history at Angermanland River (Fig. 1). That the relaxation time at this site is in accord with that for the longest wavelength components of the McConnell spectrum is strong evidence that the quality of this data set is high at longest wavelengths. To further verify the nature of the fit of the a posteriori models to the data, we present in Table 1 prior and a posteriori model fits to the characteristic relaxation times observed at the sites shown in Fig. 1, A and B.

Validation of the mantle viscosity model. To establish that the refined viscosity structure is a substantial improvement on M1, it is necessary to demonstrate that the model has predictive power. We have therefore examined rsl histories from the east coast of the North American continent and the northern coast of the South American continent. Our database of ^{14}C-dated rsl histories (7) contains time series from a large number of such locations (17 of which are shown in Fig. 1C). It has previously proven difficult to reconcile the rsl time series from the northernmost part of this region except by the introduction of an unacceptably large (20) enhancement of lithospheric thickness (7, 21). The combination of ICE-4G with the refined viscosity profile M2 fits the majority of the data from sites along this coast without any increase of lithospheric thickness from the value of 120.6 km that characterizes M1 (Fig. 4). In contrast, M1 overpredicts the rate of sea level rise at all sites along the northernmost segment of the coast. With the exception of the tightly clustered set of four locations south of New York (Brigantine, Chester River, Cape May, and Bowers, Delaware), the fit at all sites is better in M2 than in M3, the latter of which has too low a viscosity in the upper mantle and transition zone (Fig. 4). The refined model M2 was recently used (20) in conjunction with ICE-4G in an analysis of the secular trend of sea level recorded on the U.S. east coast in order to extract an improved measure of the residual signal that could be related to climate change [as discussed previously from a global perspective (22)].

Unlike the site-specific relaxation time data from locations within the LGM margins of Laurentide and Fennoscandian ice that were used to constrain the viscosity models and are only weakly dependent on deglaciation history, the rsl time series from sites that straddle the collapsing glacial forebulge, which dominates the dynamics along the U.S. east coast, depend strongly on deglaciation history as well as on the radial viscosity profile. The good fit to these

data would be destroyed if either the deglaciation model or the viscosity profile were substantially modified.

The stability of ICE-4G. To further evaluate the stability of the ICE-4G reconstruction, we considered the response to deglaciation from the perspective of global and regional maps of the present-day rate of rsl rise. To construct these predictions, we performed gravitationally and topographically self-consistent analyses (1) with the sea level equation, using ICE-4G as input along with viscosity models M1 and M2 (Fig. 5). The difference between the two predictions (Fig. 5) is largest in the region along the U.S. east coast whose dynamics are governed by the collapsing forebulge of the Laurentide ice sheet. The refinement of M1 to produce M2 thus leads to a strong modification of the response only in the geographical region in which the misfit of the M1-based theory to the observations was most pronounced. The M2-based model rectifies this misfit. For most of North America, the differences in
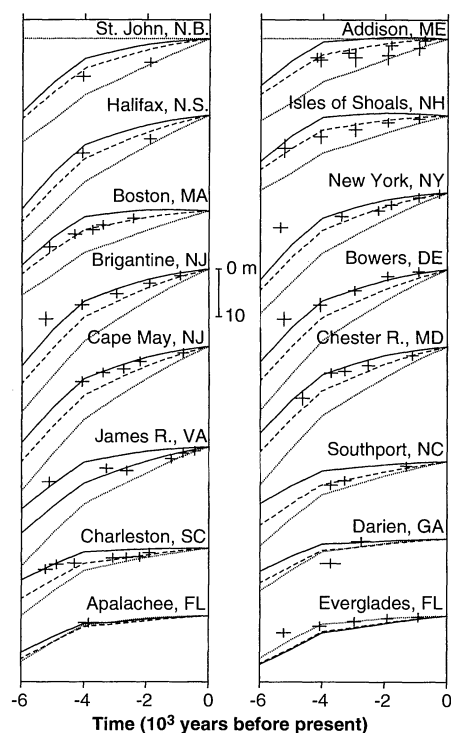

Fig. 4. Comparisons of predictions of the gravitationally and topographically self-consistent theory of postglacial rsl change with ^{14}C-dated observed histories (crosses) for 16 sites along the east coast of the continental United States (Fig. 1C). The rsl histories predicted using ICE-4G (M1) overpredict the present-day rate of rsl rise at every point along the northern position of the coast (dotted lines). The predictions produced using the combination ICE-4G (M2), on the other hand, fit the data extremely well (dashed lines). M3 (solid lines) is notably inferior, except at the four closely spaced points south of New York (Bregantine, Cape May, Chester River, and Bowers).

the predictions for the ice-covered region between M1 and M2 are small (Fig. 6), demonstrating that no significant adjustment to the ICE-4G thickness history is required to accommodate the modification to the viscosity structure.

The Fennoscandian ice sheet in northwestern Europe represents about 10% of the total ice mass in ICE-4G. In the M1-based model, the present-day rsl-fall signal over the Gulf of Bothnia reaches a maximum of 1.1 cm year^{-1}, whereas it is 0.72 cm year^{-1} for the M2-based model (Fig. 6). Because the observed maximum rate of rsl fall in this region is near 0.9 mm year^{-1} (23), the M1- (M2-) based model overpredicts (underpredicts) this rate. The reason why the present-day response at the center of Fennoscandian rebound is significantly reduced in the M2-based calculation is evident from the Fréchet kernels for the individual components of the Fennoscandian relaxation spectrum (Fig. 2). The rebound process in this region is most sensitive to upper mantle and transition zone viscosi-

ty, and it is precisely over this depth range that viscosity has been reduced in the refinement of M1 to produce M2. The isostatic adjustment process therefore proceeds more quickly in Fennoscandia in the M2-based model, leading to a significant reduction in the predicted present-day rate of rsl fall when the loading history is held fixed to ICE-4G.

Because the M2-based model now underpredicts the observed maximum present-day rate of rsl fall in Fennoscandia, the process of iterative refinement must be continued. The difference between the original LGM thickness in the ICE-4G model for northwestern Europe and that for the refinement required to accurately predict the present-day observed rate of rsl fall over Fennoscandia using the M2 viscosity profile is shown in Fig. 7A. The adjustment to the ICE-4G thickness history required to eliminate the misfit is very modest over most of the region, reaching a maximum of 800 m in a localized region centered over the head of the Gulf of Bothnia. As a fraction of the total mass of

Fennoscandian ice in ICE-4G, the increase in the ice load is about 15%. From a global perspective, the increased eustatic rise effected by the adjustment to ICE-4G is 1.6 m, less than 2% of the ICE-4G total. The present-day predicted rate of rsl fall for the Fennoscandian region according to the thickness history that incorporates the required adjustment to ICE-4G and the M2 viscosity model (Fig. 7B) now satisfies the observational constraints (23).

Because the ICE-4G model is highly stable under refinement of M1 to produce M2, it is clear that the previously produced paleotopographic maps (1) now in use by the Paleoclimate Model Intercomparison Project require no significant modification.

Mantle viscosity. Several earlier radial viscosity models [see (24)] also based on interpretations of GIA data (Fig. 8A) are clearly incompatible with models M2 and M3 in that they are characterized by excessively high viscosity in at least the uppermost part of the lower mantle. Detailed analyses of these regionally derived comparison

Fig. 5 (right). Global predictions of the present-day rate of rsl rise for M1 and M2 and the difference between those predictions (M1 − M2). The largest deviation between the predictions of these two models occurs in the region of postglacial forebulge collapse along the east coast of North America. The diminished rate of rsl rise in this region predicted by the M2-based model, which allows the ICE-4G deglaciation history to achieve the high-quality fit to the observations shown in Fig. 4. **Table 1 (below).** Site-dependent relaxation times from Hudson Bay, Arctic Canada, and Fennoscandia. T_o denotes the observed relaxation times (with standard errors) (which were estimated by a Monte Carlo procedure), and T_s denotes the predicted relaxation times based on M1. T_f denotes the relaxation times for the final model obtained by formal inversion of the complete data set, which includes the McConnell relaxation spectrum and the two rotational constraints as well as the site-specific relaxation times listed here. Unif., uniform viscosity model.

M1

M2

M1 − M2

Sea level rise (mm/year)

Sites	T_o (10^3 years)	T_s (10^3 years)		T_f (10^3 years)	
	a ± b	M1	Unif.	M2	M3
Hudson Bay					
James Bay	3.64 ± 0.68	6.69	4.66	5.01	4.55
Ottawa Island	3.06 ± 0.52	4.92	2.50	4.16	3.67
Ungava Pen.	3.34 ± 0.83	4.10	1.90	4.09	3.70
Richmond Gulf	7.23 ± 3.18	5.84	3.64	4.62	4.04
Churchill	5.70 ± 2.02	5.23	3.09	4.66	4.18
Keewatin	5.73 ± 4.60	4.99	3.13	4.47	4.10
Southampton (Is)	4.69 ± 1.61	4.60	2.55	4.24	3.89
Arctic Canada					
Sam Ford Fiord	5.35 ± 3.49	4.32	3.10	5.28	5.56
Tay Sound	2.77 ± 1.29	4.20	2.75	4.57	5.04
Milne Inlet	4.35 ± 2.52	4.54	3.18	4.66	5.11
Baird Pen.	4.50 ± 1.50	5.62	4.42	5.64	6.00
Ipik Bay	2.95 ± 0.67	6.19	4.83	5.95	6.31
Igloolik Is.	4.63 ± 1.94	5.40	3.99	4.99	5.10
Bathurst Inlet	4.93 ± 2.14	5.66	3.84	5.03	4.83
Somerset Is.	5.38 ± 4.00	4.25	2.37	4.62	4.98
Cape Storm	5.57 ± 2.11	5.00	3.68	4.70	5.36
Bay Fiord	5.82 ± 3.26	6.33	4.97	5.08	5.73
Fennoscandia					
Ingoy	6.75 ± 4.18	6.90	7.01	6.22	4.65
Bjugn	5.51 ± 2.36	9.71	7.06	5.70	5.49
Oslo	6.08 ± 1.57	8.26	6.44	5.34	5.62
Fjallbacka	5.60 ± 1.77	12.00	8.63	7.82	7.35
Stockholm	3.25 ± 0.73	8.45	6.34	5.75	4.95
Angermanland	4.94 ± 1.41	8.57	6.52	5.27	5.08
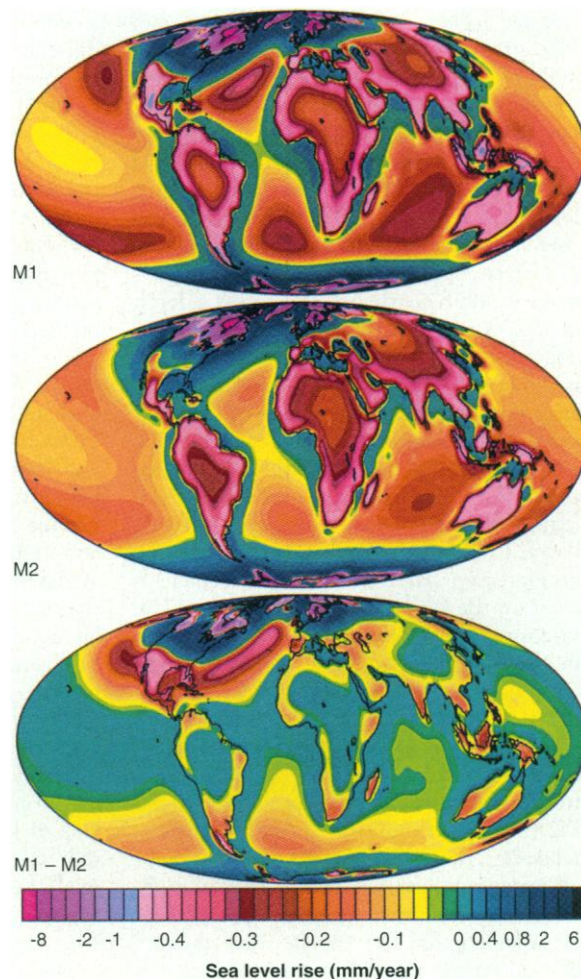
models using the formal theory of Bayesian inference (10) have shown them to be suboptimal. Our work demonstrates that such regionally distinct models are not required to reconcile the observational data, implying that the GIA phenomenon is relatively insensitive to the lateral viscosity variations that must exist in the convecting mantle as

a result of the thermally activated nature of the solid-state creep process. Of these regionally derived models, the closest to the M2-M3 average is that deduced by Lambeck et al. [LJN (24)] on the basis of trial and error fits to Fennoscandian rebound data. Although this model is unacceptably stiff in the upper 500 km of the lower mantle, the vis-

cosity in the upper mantle and transition zone, which controls the response in Fennoscandia according to the Fréchet derivatives (Fig. 3), is essentially the same as that in the M2-M3 average profile. It is notable that all of the comparison models (Fig. 8A) are similar to M2-M3 in this region; only in the lower mantle are they unacceptably stiff according to these formal analyses.

Radial viscosity models based on analysis of nonhydrostatic geoid (NHG) anomalies related to the process of mantle convection have also been produced (Fig. 8B), and the relation of these to the GIA-derived results is especially important. The earliest of such models (such as HR in Fig. 8B) was characterized by an increase in viscosity by a factor of 100 across the 660-km seismic discontinuity. More recent analyses of the same data with improved theoretical models have demonstrated that such extreme variations of viscosity are not required, although these models (RW and FPDW on Fig. 8B) are at least superficially discordant with our inferences based on GIA analysis. That such disagreement is only superficial, however, is demonstrated if we superimpose a rescaled version of the most recent NHG-derived model (18) and M2 (Fig. 8C). In this context, rescaling simply involves multiplication of the viscosity profile by a constant (in this case, 0.37), a modification that does not impact the fit of theory to the NHG data (18).
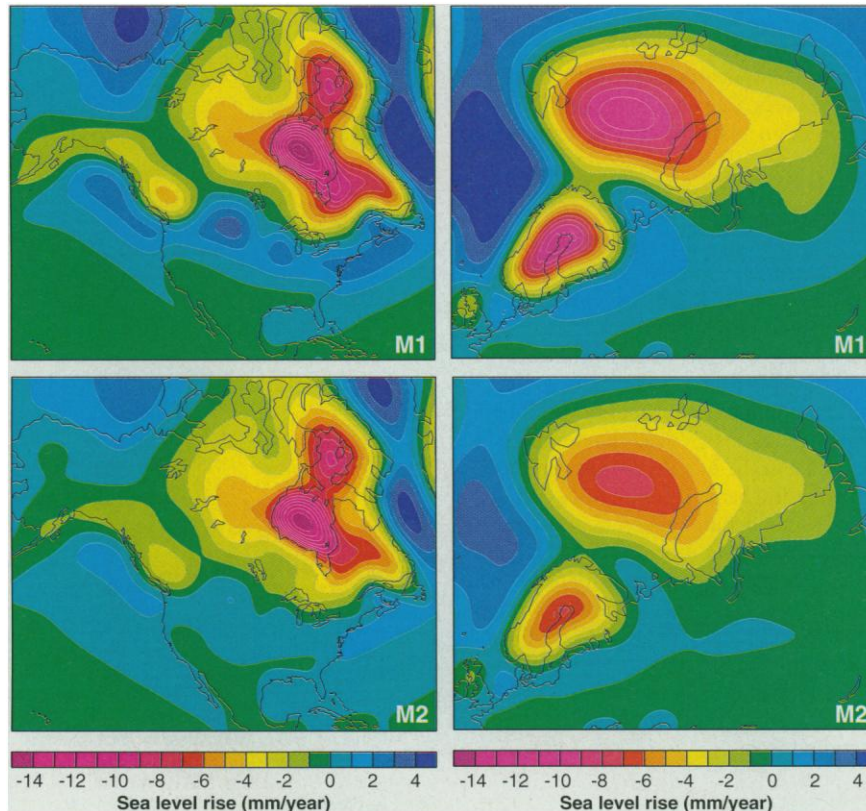

Fig. 6. Predictions of present-day rsl rise for the regions of North America and northwestern Europe that were covered with ice at the LGM. For each region, the predicted rates of rsl rise are shown for both M1 and M2.
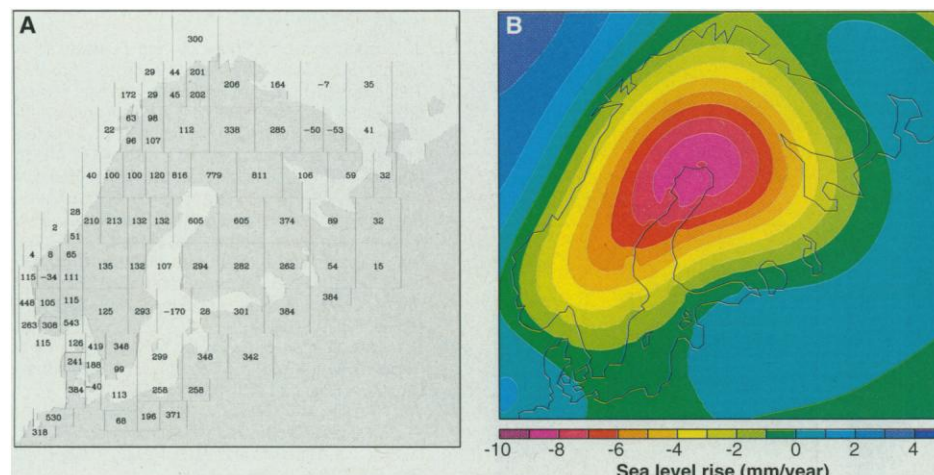

Fig. 7. (**A**) The LGM adjustment to ice sheet thickness (in meters) that must be introduced to correct the small misfit of ICE-4G (M2) to observations of the present-day rate of uplift of the land relative to the sea in Fennoscandia. (**B**) The present-day rate of rsl rise over Fennoscandia predicted with the modification to ICE-4G shown in (A).
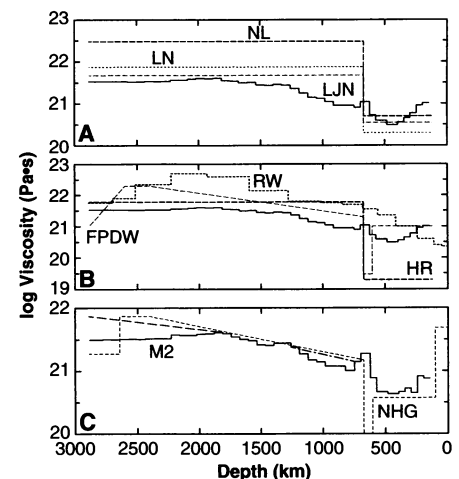

Fig. 8. (**A**) The M2-M3 average viscosity profile (solid line) compared to three alternative viscosity models previously inferred on the basis of glacial isostatic adjustment data. (**B**) The M2-M3 average viscosity profile (solid line) compared to three alternative viscosity models previously inferred on the basis of nonhydrostatic geoid anomaly data. (**C**) The M2 viscosity profile compared with the profile recently inferred on the basis of nonhydrostatic geoid (NHG) analyses (18) in which the latter profile has been rescaled by dividing the viscosity at each depth by a factor of 2.7. See (24) for curve labels and citations.
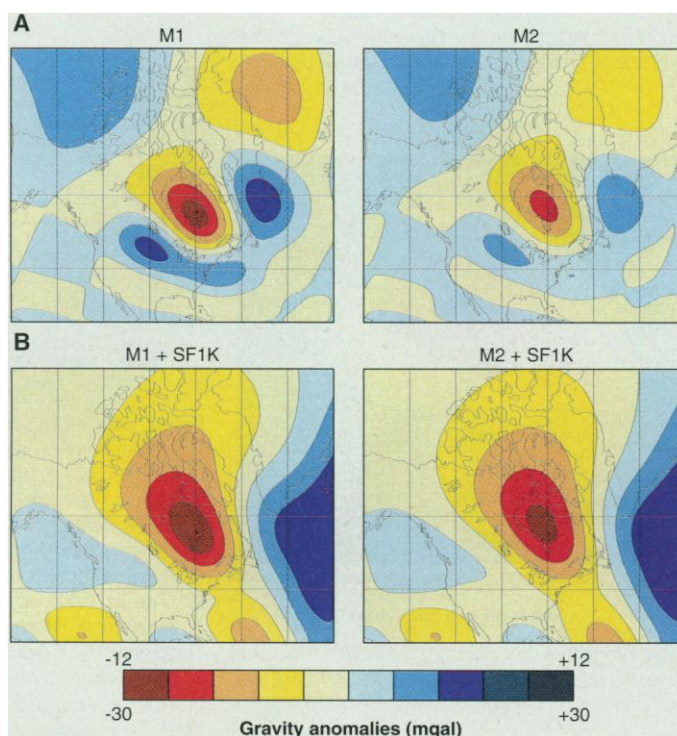
Models RW and FPDW (Fig. 8B) can be similarly rescaled to bring them into equally close accord with the M2-M3 average deduced on the basis of our GIA analyses. Also shown on Fig. 8C as heavy dashed lines are the modifications to M2 that are effected by specific modifications to the input data set. The deepest of the regions so delineated is one in which viscosity is elevated so as to overlap more precisely with the NHG result when account is taken of the contamination of the rotational data that may be caused by the ongoing rise of mean global sea level (11, 12). In the shallowest of these regions, immediately beneath the 660-km discontinuity, the slight diminution of viscosity below that in M1 and the NHG result may be eliminated by constraining the GIA-derived viscosity model so as to predict the maximum free-air gravity anomaly that is compatible with the rsl observations. The thin layer of low viscosity in the NHG-derived result does not represent a significant departure from the GIA profile, because the GIA data are not particularly sensitive to its presence.

That GIA- and NHG-derived radial viscosity profiles have been shown herein to be fully compatible [see also (11, 12)] is extremely important. This result goes to the heart of our understanding of mantle rheology, for it implies that the solid-state creep mechanisms that govern mantle flow are not significantly transient. The viscosity that governs the relatively short time scale GIA process is essentially the same as the viscosity that governs the long time scale

mantle convection process that is required to support observed NHG anomalies. Because non-Newtonian creep mechanisms are by necessity transient, our result suggests that viscous mantle dynamics may be essentially Newtonian in the sublithospheric region where temperatures approach the melting temperature. This conclusion is highly significant.

That the GIA- and NHG-derived viscosity structures are fully compatible also enables resolution of what has been recognized as a profound geophysical paradox (25) related to the origin of the free-air gravity anomaly over the Laurentian platform that is centered on Hudson Bay. The maximum predicted present-day free-air gravity anomalies over this region (Fig. 9) for the M1- and M2-based models of GIA in the spherical harmonic degree range from 2 to 8 based on calculations that account for the influence of past cycles of glaciation and deglaciation (26) are, respectively, 11 and 8 mgal, whereas the observed anomaly in this degree range (25) is near 28 mgal. The dominant contribution to the free-air gravity anomaly over Laurentia must therefore lie in the mantle convection process rather than in glacial isostatic disequilibrium. On the basis of detailed theoretical analyses in which the results of seismic tomography are used to constrain the internal density field, the convection contribution can be accurately modeled (18, 27). The total anomalies derived from the superposition of these two contributions (Fig. 9) fit the observations (25) extremely well and thus settle this additional outstanding issue.

REFERENCES AND NOTES

1. W. R. Peltier, *Science* **265**, 195 (1994); *ibid.* **267**, 536 (1995).
2. _____, *Rev. Geophys. Space Phys.* **12**, 649 (1974); W. E. Farrell and J. A. Clark, *Geophys. J. R. Astron. Soc.* **46**, 647 (1976); W. R. Peltier and J. T. Andrews, *ibid.*, p. 605; W. R. Peltier, W. E. Farrell, J. A. Clark, *Tectonophysics* **50**, 81 (1978); J. A. Clark, W. E. Farrell, W. R. Peltier, *Quat. Res.* **9**, 265 (1978); W. R. Peltier, *J. Geophys. Res.* **90**, 9411 (1985); P. Wu and W. R. Peltier, *Geophys. J. R. Astron. Soc.* **70**, 435 (1982); P. Wu and W. R. Peltier, *ibid.* **76**, 202 (1984); J. X. Mitrovica and W. R. Peltier, *J. Geophys. Res.* **96**, 20053 (1991).
3. A. M. Dziewonski and D. L. Anderson, *Earth Planet. Sci. Lett.* **25**, 297 (1978).
4. D. Han and J. Wahr, *Geophys. J. Int.* **120**, 287 (1995).
5. R. A. Kerr, *Science* **265**, 189 (1994).
6. W. R. Peltier, R. Drummond, A. M. Tushingham, *Geophys. J. R. Astron. Soc.* **87**, 79 (1986).
7. A. M. Tushingham and W. R. Peltier, *J. Geophys. Res.* **97**, 3285 (1992).
8. N. A. Haskell, *Am. J. Sci.* **33**, 22 (1937).
9. CLIMAP Project Members, *Science* **191**, 1131 (1976); *Geol. Soc. Am. Map Ser. MC-36* (Geological Society of America, Washington, DC, 1981).
10. J. X. Mitrovica and W. R. Peltier, *Geophys. J. Int.* **104**, 267 (1991); *ibid.* **114**, 45 (1993); *Geophys. Res. Lett.* **20**, 2183 (1993); *Geophys. J. Int.* **122**, 353 (1995).
11. W. R. Peltier and X. Jiang, *J. Geophys. Res.* **101**, 3269 (1996).
12. _____, *Geophys. Res. Lett.* **23**, 503 (1996).
13. A. Tarantola and B. Vallette, *J. Geophys.* **50**, 159 (1982); *Rev. Geophys. Space Phys.* **20**, 219 (1982); G. E. Backus, *Geophys. J. R. Astron. Soc.* **92**, 125 (1988).
14. R. K. McConnell, *J. Geophys. Res.* **73**, 7089 (1968).
15. W. R. Peltier, *Geophys. J. R. Astron. Soc.* **46**, 669 (1976).
16. B. H. Hager, *J. Geophys. Res.* **89**, 6003 (1984); M. A. Richards and B. H. Hager, *ibid.*, p. 5987; Y. Ricard and C. Vigny, *ibid.* **94**, 17543 (1989).
17. L. M. Cathles, *The Viscosity of the Earth's Mantle* (Princeton Univ. Press, Princeton, NJ, 1975); W. Fjeldskaar and L. M. Cathles, in *Glacial Isostasy, Sea Level and Mantle Rheology*, R. Sabadini, K. Lambeck, E. Boschi, Eds. (NATO ASI Ser. 334, Kluwer, Dordrecht, Netherlands, 1991), pp. 1–20.
18. G. Pari and W. R. Peltier, *J. Geophys. Res.* **100**, 12731 (1995).
19. A. M. Forte, W. R. Peltier, A. M. Dziewonski, R. L. Woodward, *Geophys. Res. Lett.* **20**, 225 (1993).
20. W. R. Peltier, *ibid.* **23**, 717 (1996).
21. _____, *J. Geophys. Res.* **89**, 303 (1984).
22. _____ and A. M. Tushingham, *Science* **244**, 806 (1989).
23. J. Donner, in *Earth Rheology and Eustasy*, N.-A. Morner, Ed. (Wiley, New York, 1980), pp. 285–293.
24. The viscosity models to which the rebound derived profiles are compared in Fig. 8 are derived from the following references. LJN: K. Lambeck, P. Johnston, M. Nakada, *Geophys. J. Int.* **103**, 451 (1990); NL: M. Nakada and K. Lambeck, *ibid.* **96**, 497 (1989); LN: _____, in *Glacial Isostasy, Sea Level and Mantle Rheology*, R. Sabadini, K. Lambeck, E. Boschi, Eds. (Kluwer, Dordrecht, Netherlands, 1991), pp. 79–94; RW: Y. Ricard and B. Wuming, *Geophys. J. Int.* **105**, 561 (1991); HR: B. H. Hager and M. A. Richards, *Philos. Trans. R. Soc. London Ser. A* **328**, 309 (1989); FPDW: (19).
25. R. I. Walcott, *Can. J. Earth Sci.* **7**, 716 (1970); W. R. Peltier, A. M. Forte, J. X. Mitrovica, A. M. Dziewonski, *Geophys. Res. Lett.* **19**, 1555 (1992).
26. W. R. Peltier, *Adv. Geophys.* **24**, 1 (1982); P. Wu and W. R. Peltier, *Geophys. J. R. Astron. Soc.* **74**, 377 (1983); J. X. Mitrovica and W. R. Peltier, *J. Geophys. Res.* **94**, 13651 (1989).
27. G. Pari and W. R. Peltier, *J. Geophys. Res.*, in press.
28. I am indebted to R. Drummond, X. Jiang, and G. Pari for their input to this work.

Fig. 9. (**A**) Free-air gravity anomalies over the Laurentian platform based on GIA analysis (25) using viscosity models M1 and M2 and computed in the range of spherical harmonic degree from 2 through 8. (**B**) Total anomalies from the superposition of that caused by the GIA process and that caused by mantle convection computed using mantle tomography model SF1K (27). The latter process dominates the observed signal described in (25).